Negative-Stiffness Inclusions as a Platform for Real-Time Tunable Phononic Metamaterials

L. Salari-Sharif, B. Haghpanah, A. Guell Izard, M. Tootkaboni, and L. Valdevit

Phys. Rev. Applied **11**, 024062 — Published 25 February 2019

DOI: 10.1103/PhysRevApplied.11.024062

Negative Stiffness Inclusions as a Platform for Real-Time Tunable Phononic Metamaterials

L. Salari-Sharif[1,2], B. Haghpanah[1], A. Guell Izard[1], M. Tootkaboni[2], L. Valdevit[1,3]*

[1]Mechanical and Aerospace Engineering Department, University of California, Irvine

[2]Civil and Environmental Engineering Department, University of Massachusetts, Dartmouth

[3]Materials Science and Engineering Department, University of California, Irvine

Abstract

We propose an approach for real-time manipulation of low-frequency phononic band gaps in a metamaterial without affecting the material geometry, microarchitecture, or the crystal structure of the base material. Metamaterials with tunable band gaps are realized by introducing periodically arranged negative stiffness inclusions, the modulus of which can be varied in time in order to modify the metamaterial macroscopic stiffness in certain directions, without bringing the material to the point of elastic instability or inducing extreme geometric change. The evolution of band gaps is investigated numerically, and the proposed concept is verified experimentally in a lattice prototype with magnetic elements functioning as negative stiffness units. Design guidelines for achieving real-time tunable phononic band gap are also presented.

[*] Corresponding author (valdevit@uci.edu)

1. Introduction

Various strategies exist in the literature to create and widen band gaps (i.e., frequency ranges of strong attenuation of propagating waves within a material at any polarization and any incident angle) in crystalline materials as well as photonic, phononic and acoustic metamaterials [1–3]. For example, reducing the crystal symmetry of a FCC lattice by introduction of a two-point basis set could result in a non-Bravais diamond cubic structure with reduced band degeneracies, thus introducing band gaps [4, 5]. Photonic and phononic band gaps in metamaterials are commonly formed by Bragg scattering [6, 7], i.e., the establishment of destructive interference between transmitted and reflected waves. Bragg-type band gaps appear about an angular frequency ω of the order of c/a, where a is the unit cell size and c is the wave speed in the medium [5]. This relationship necessitates a sufficiently large lattice size for creation of a low frequency band gap. For instance, phononic crystals with periodicities on the order of meters to tens of centimeters are required to forbid the propagation of mechanical waves with frequencies in the range 20-2,000 Hz [1]. Locally resonant band gaps [8–11], on the other hand, arise typically in the vicinity of the natural frequencies of the resonating units, and can be experimentally realized at frequencies up to two orders of magnitude lower than the typical Bragg limit of a material with equal lattice constant [12].

Based on these physical considerations, various techniques have been proposed in order to obtain real-time *tunable* frequency band gaps. Such a technology, if successfully developed and implemented, could enable important phononic, photonic or acoustic applications in active cloaking [13], wave guiding [14, 15], active noise reduction [16–18], super-lensing [19, 20], and acoustic mirrors [21, 22]. The literature on this subject includes recent efforts to create or enlarge acoustic band gaps through application of macroscopic deformation fields within a elastomeric metamaterial, of either pre- [19, 23, 24] or post- [25–28] elastic bifurcation (buckling) nature. The induced change in the size and/or shape of the unit cell in turn modifies the Bragg scattering or local resonance characteristics of the phononic crystal. The requirement for extreme geometrical change in order to achieve tunability even appears in magneto-electro-elastic phononic crystals, where a coupling between magnetic, electric and elastic phenomena is responsible for creation or widening of band gaps [3, 29–33]. All these approaches share a few critical limitations. Inducing deformations sufficiently large to yield tangible phononic change in a material is inconvenient and energetically costly (especially if the material is load bearing). Moreover, geometric conversions at frequencies high enough for active filtration of incident waves with time-varying frequencies could lead to undesirable vibrational complications. An alternative proposed approach towards phononic tunability stems from thermally induced material phase transitions accompanied by changes in bulk acoustic velocities [34–37]. In these methods, the achievable response time for tunability is somewhat restricted by physical constraints on heat flow rate within the phononic crystal[38].

2. General framework for tunable negative-stiffness-based phononic metamaterials

Here, we propose a novel and convenient method for real-time manipulation of low-frequency complete phononic band gaps in an active composite material. The proposed material consists of an elastic matrix encompassing negative stiffness (NS) inclusions, the modulus of which can be actively tuned in order to locally reduce the material stiffness at controlled periodic locations and in certain directions, thus yielding changes in its phononic response, including both the width and locations of frequency band gaps. Interestingly, a selective band gap tuning for quasi-longitudinal and quasi-transverse waves is also shown to be possible. As no large geometric changes in the material is required, the actuation time depends on the physics behind the implementation of the tunable NS phase. We propose to use electromagnets for this purpose, thus enabling actuation times as fast as a few milliseconds [39]. If piezoelectric actuators are used in lieu of magnets, response times of the order of microseconds can be achieved [40, 41].

As the addition of NS inclusions to a matrix could lead to loss of mechanical stability of the resulting metamaterial, it is imperative to start by investigating stability considerations. The stability of composite materials containing NS elements has been the subject of various studies[42–44]. Kochmann and Drugan [43] showed that, assuming strong ellipticity for all the constituents including the NS inclusions, the critical condition for positive definiteness of the fourth order macroscopic elasticity tensor of an isotropic composite material, and hence its macroscopic stability, is given by $\overline{K} > 0$, where $\overline{K}$ is the effective bulk modulus of the composite material. As the Hashin-Shtrickman solution provides an analytical bound for the bulk modulus of a two-phase composite [45, 46], this condition translates into a minimum allowable bulk modulus for the NS inclusions, k^{cr}, i.e.:

$$k^{cr} = -\frac{k_m G_m \left(1-f\right)}{k_m + G_m \left(1-f\right)} \tag{1}$$

where k_m and G_m are the bulk modulus and shear stiffness of the matrix, and f is the volume fraction of the NS inclusions. NS intensities past the critical value given in (1) will lead to instabilities in the composite medium under generalized (mixed) boundary conditions [47]. As will be seen later, considerable changes in the phononic response of the composite material begin to emerge at NS intensities notably smaller in magnitude than k^{cr}. In the current work, the condition on simultaneous structural (macroscopic) and microscopic stabilities is also rigorously satisfied by ensuring the positiveness of all Bloch eigenfrequencies corresponding to elastic waves of various directions and wavelengths propagating within the periodic elastic medium (i.e. all non-zero wave vectors within the Brillouin zone of the phononic material)[48].

As a schematic illustration of this concept, consider the phononic crystal depicted in Figure 1a, composed of a periodic arrangement of three phases: an elastic matrix (in black), circular-shaped NS inclusions (in gray when active), and square-shaped voids. We assume that the negative bulk modulus of the NS inclusions can be varied in real time in the range $k_{cr} < k < 0$. In order to calculate the band structure of the phononic crystal, we use a finite element (FE) model of the unit cell subjected to Bloch boundary conditions (see Appendix 2 for details) [47,48]. As most commercial FE software packages do not support material models with negative stiffness, the NS inclusions are numerically modeled as circular voids, with diametrically opposed points on the circumference connected by linear springs with negative spring constant. The number of connectors and their spring constant are chosen to simulate the global effect of the prescribed NS negative bulk modulus. The bulk modulus, k, of the NS inclusions is incrementally decreased from zero to k^{cr}, and the changes in the band structure are examined. The band structure diagram of the phononic crystal when the NS inclusions have a zero intensity (i.e. are inactive) are shown in Figure 1b left. By increasing the intensity of the NS inclusions, the normal elements of the stiffness matrix in X and Y directions are decreased, altering the location and width of the frequency band gap as shown in Figure 1b right. Notice that while the frequency gap is lowered by activating the NS elements, its width is not significantly expanded. In other words, all the bands have shifted to lower frequencies by similar amounts.

A more efficient actuation strategy can be devised if the architected phononic crystal is designed according to two important criteria: (i) actuation of the NS elements results in decreasing longitudinal stiffness in (arbitrary) direction, X, without decreasing the shear stiffness of the material, G, in the same direction; and (ii) the macroscopic Poisson's ratio of the material along X is near zero. Condition (i) satisfies two important physical functions. First, it ensures positive-definiteness of the elasticity tensor (for a two-dimensional isotropic linear elastic material the sufficient and necessary conditions for positive definiteness are $G > 0$ and $-1 < \nu < 1$) [49, 50]. Second, it ensures that, within the band-diagram of the real-time phononic material with NS inclusions, only the dispersion curves relating to predominantly longitudinal polarization are lowered while the transverse-type waves are almost unaffected by activations of the inclusions. Without this selectivity in suppression of eigensolutions, all existing modal frequencies will decrease together and the existing degeneracies will merely shift from a high frequency state to a lower one (as in 2D and 3D phononic crystals the longitudinal and transverse vibrations of the medium are coupled, in what follows we use the prefix 'quasi' to denote polarizations that are primarily horizontal or vertical [51]). Condition (ii) can be inferred based on the Bloch-periodic boundary condition in phononic crystals[52]

$$u_k(\boldsymbol{x} + \boldsymbol{r}, t) = u_k(\boldsymbol{x}, t)e^{i\boldsymbol{k}\cdot\boldsymbol{r}} \tag{2}$$

where $\boldsymbol{k}$, $\boldsymbol{x}$ and $\boldsymbol{r}$ denote the wave vector, the (Cartesian) position vector, and the periodicity vector, respectively, and $\boldsymbol{u}_k(\boldsymbol{x}, t)$ is a complex periodic vector-valued function with the same spatial period as the phononic crystal. Equation (2) requires all sets of periodic points within the material which are relatively located perpendicular to the direction of propagation of the incident wave (i.e. $\boldsymbol{k} \cdot \boldsymbol{r} = 0$) to have equal displacements. The set of conditions (i) and (ii) essentially implies that the proposed material hosting a propagating wave in X needs to satisfy reduced longitudinal stiffness in X quasi-statically, whilst accommodating near-zero lateral expansion in Y as required by the Bloch theorem. It is speculated that the described approach for tunable phononic response would be most effective at relatively low wave frequencies, where the existence of NS inclusions results in decreased quasi-static stiffness of the material in the desired directions. Such hypothesis is consistent with the observation that the proposed method yields little to virtually no change in the band structure response of the phononic material in the high frequency domain.

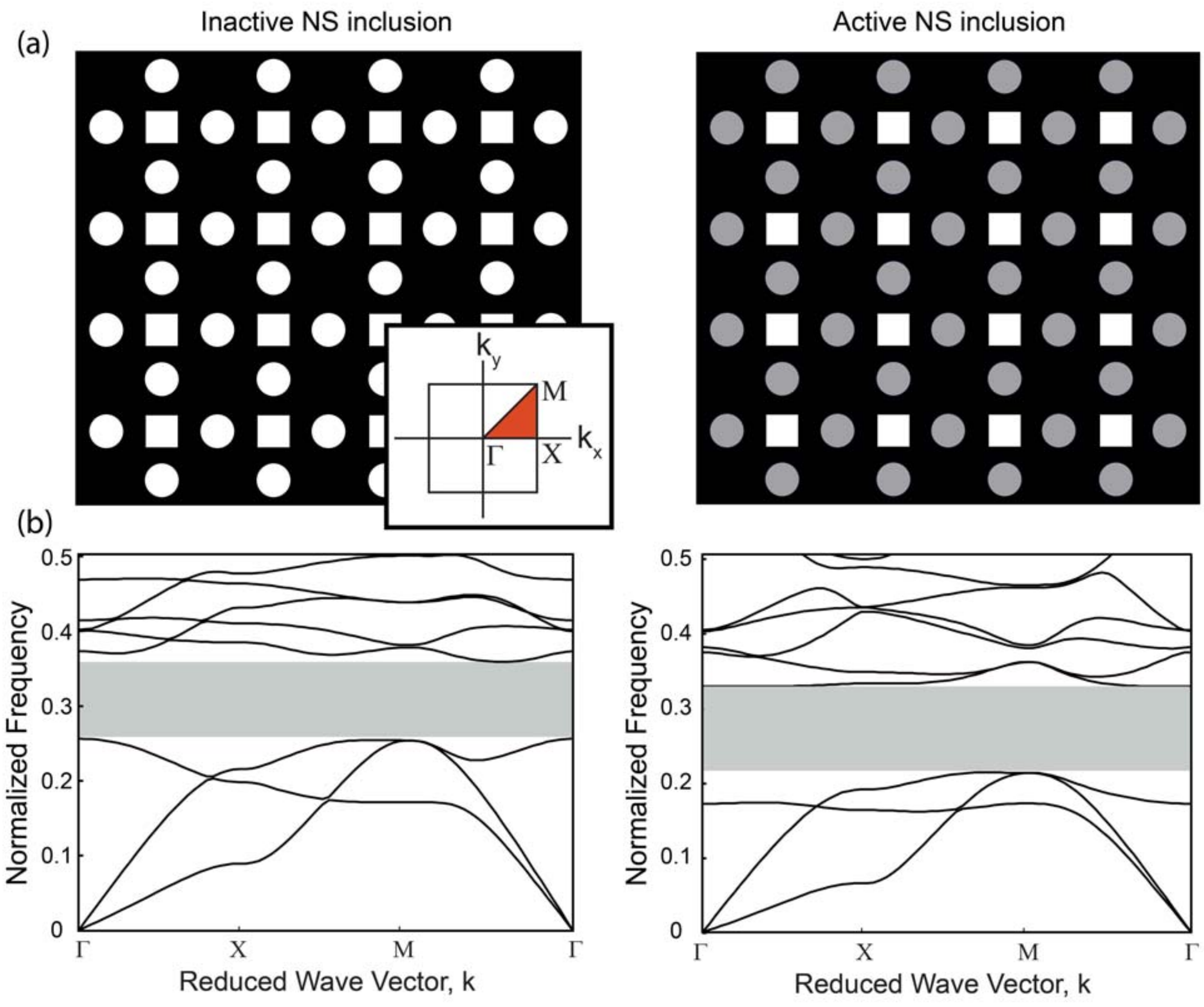

Figure 1. (a) Schematic of a 2D tunable phononic crystal with NS inclusions in the inactive (left) and active (right) states. The black, white and grey colors represent matrix, void, and active NS inclusions, respectively. (b) Dispersion relations for the phononic crystal in the inactive (left) and active (right) states.

3. Physical implementation in a lattice material configuration

With the general concepts clarified and demonstrated, we now apply the aforementioned conditions simultaneously to a physical implementation consisting of 1D and 2D lattice materials incorporating electro-magnets. These implementations are both physically realizable and particularly instructive.

A building block for the proposed tessellated structures, shown in Figure 2a, consists of a diamond-shaped frame, two vertical bars extended inward from the two opposite vertices of the frame and attached to two electromagnets facing the center of the unit cell, and two bars extended outward horizontally from the two other corners of the frame with their outer ends denoted by nodes A and B. The axial stiffness of the building block measured between points A and B, denoted by K_x, can be decreased by applying a voltage to the two attracting electromagnets at the center of the unit cell. The attractive electromagnetic force between the two electromagnets as a function of their distance for different values of applied voltage is given in Figure 2b. Also shown in this figure by a dashed line is the load-displacement response between nodes C and D when the electromagnets are inactive, whose slope is denoted by K_y (at $\theta = 45^{\circ}$ the diamond frame becomes square, and $K_x = K_y$ since the unit cell is kinematically indeterminate based on Maxwell's rule[47]). After activation of the electromagnets, a theoretically zero-stiffness (albeit unstable) state, marked by an asterisk in Figure 2a, is achieved if the electromagnetic force–distance curve is chosen to be tangent to the dashed line. In the general case, the axial stiffness of the unit cell with an active set of electromagnets resulting in a NS of k^*, can be expressed by $K_{eq}(V) = K_y\left(1 - \frac{k^*(V)}{K_x}\right)$, where V is the applied voltage (see Appendix 1). The value of applied voltage can be changed to tune, in real-time, the overall stiffness of the phononic lattice. The concept of modulating stiffness via actuation of electromagnets was verified numerically, through the finite elements method, and experimentally, on a unit cell consisting of a Poly(lactic acid) (PLA) 3D printed frame with two embedded electromagnets (Figure 2a). The experimental force-separation curve for the magnets was measured by separating a pair of magnets initially in contact, in a quasi-static displacement-controlled test, as a function of the applied voltage (Figure 2b). As noted in Appendix 1, these measurements allow extraction of k^*. The load-displacement response of the diamond frame was obtained by compressing the frame along the A-B direction, for two different values of the applied voltage (corresponding to voltage equal to zero and to voltage offsetting the elastic stiffness of the frame). In the FE model (solved with Abaqus/Standard), the interactions between the magnets is modeled with a non-linear spring connector element, with the same force-separation law measured experimentally. The numerical and experimental force-displacement response of the unit cell with the electromagnets in the inactive and active states are given in Figure 2c, and show excellent agreement. The initial slope of the force-displacement response decreases significantly by activation of the electromagnets. Notice that at large displacements the tangential stiffness of the two modes converge.

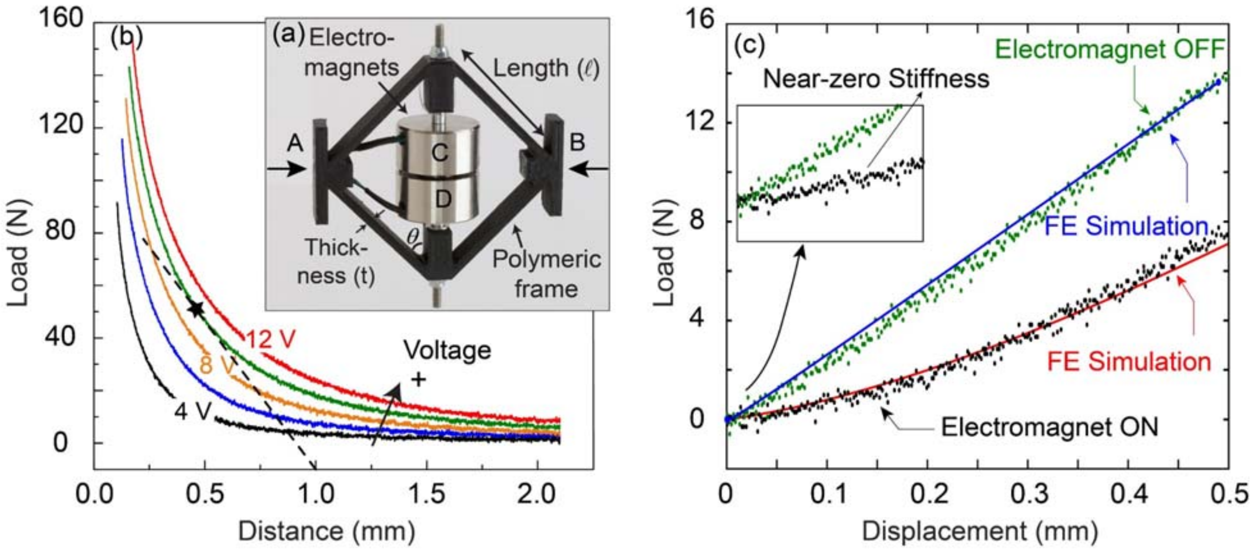

Figure 2. (a) Schematic and fabricated unit cell of a tunable phononic metamaterial, activated by a pair of attracting electromagnets in the middle of the unit cell. (b) The magnetic (colored curves for different applied voltages) and elastic (dashed line) force-distance profile between two electromagnets. (c) The force-displacement response of the proposed unit-cell under external uniaxial quasi-static loading. The green and black dots show the experimental results for inactive and active electromagnets, respectively. The solid lines show the finite element results.

3.1 One-dimensional tessellation

The first design studied is an infinite one-dimensional tessellation, shown in Figure 3c. In order to obtain the band structure of the proposed phononic material, the Bloch boundary condition given in Equation (2) was applied to the unit cell of the structure (see Appendix 2). To produce a change in the phononic response, the absolute value of the negative stiffness was swept incrementally from zero (electromagnet OFF) to the opposite of the stiffness of the frame. For each NS intensity, the eigenfrequencies for a varying set of wave vectors describing the irreducible Brillouin zone associated with the phononic crystal were recorded. The band structure for this structure is shown in Figure 3d (left) when the NS elements are inactive. Figure 3e (left) shows the band structure when the NS intensity of the electromagnets equals ~70% of the stiffness of the polymeric frame. The dispersion curves within the frequency range shown are labeled by numbers 1 through 4; note that the modes are *crossing,* as opposed to veering. The calculated mode shapes indicate that the first and second curves correspond to quasi-transverse and quasi-longitudinal modes, respectively. As shown in Figure 3e (left), activation of the electromagnets can eventually result in a complete suppression of the quasi-longitudinal mode (curve 2 in Figure 3d (left)), and therefore in the instability of the structure. Note that in the band diagram of the activated phononic crystal shown in Figure 3e (left), the difference between the maximum frequency of the quasi-transverse mode (curve 1 in Figure 3d (left)) and the minimum frequency of the mode 3 with a predominately shear component determines the width of the band gap formed at the frequency range presented. Figure 4**Error! Reference source not found.** shows the relationship between the width of the bandgap formed versus the intensity of the negative stiffness due to activated electromagnets, normalized by the axial stiffness of the frame, $\bar{k} = \frac{(\partial F / \partial x)_{magnet}}{K_x}$. As shown in this figure, no bandgap is formed in the range $\bar{k} = 0$ to $\bar{k} = 0.5$. At $\bar{k}$~0.6 the maximum width of bandgap is achieved when the peaks of curves 1 and 2 coincide, and increasing the voltage after this point dose not lead to any further advantage. This example clearly shows that, in order to achieve the maximum bandgap, a complete loss of stiffness of the structure is not necessary: in the case presented, decreasing the stiffness by 65% was sufficient to yield maximum achievable bandgap without bringing the structure to the point of instability.

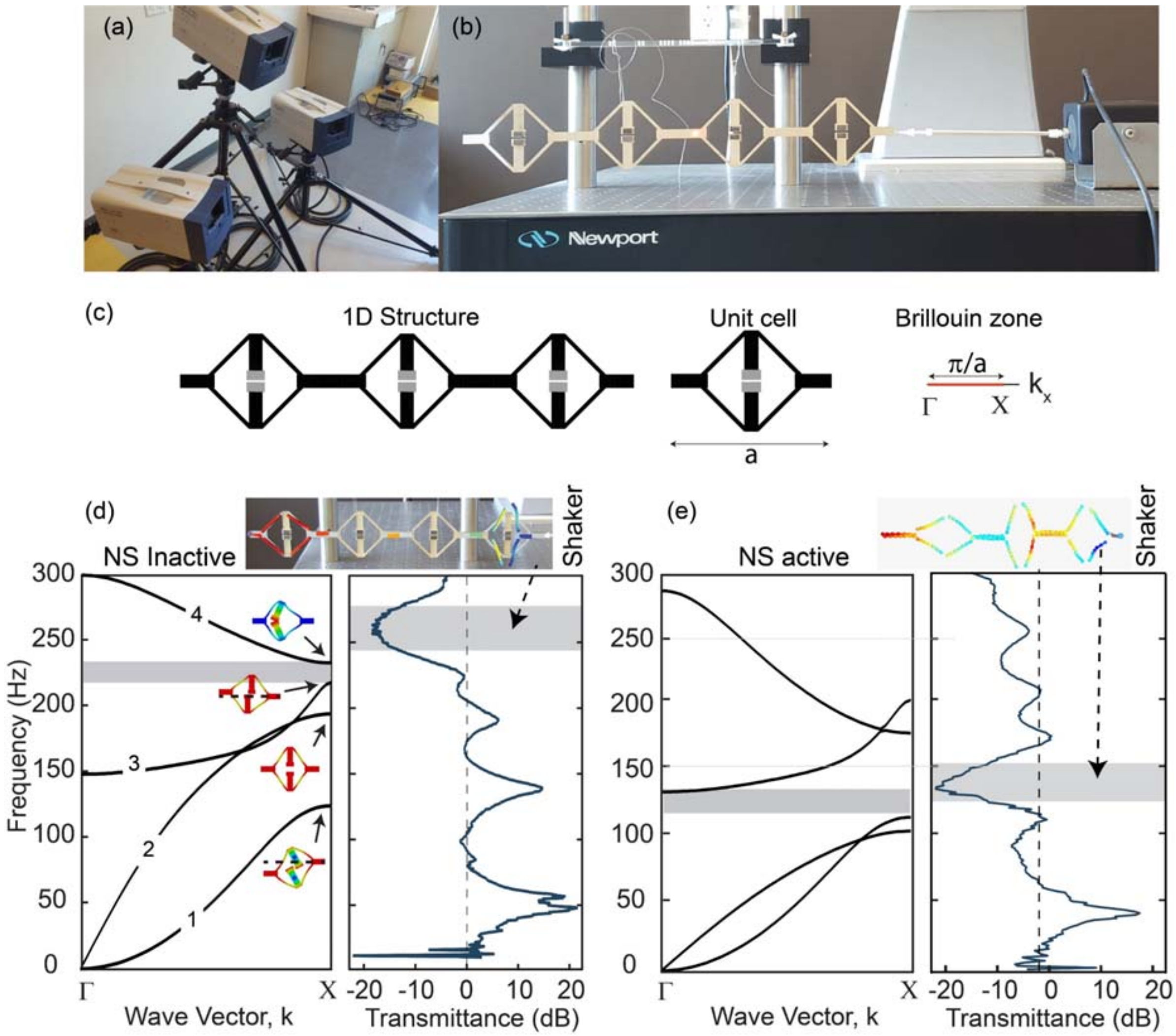

Figure 3. (a) 3D Laser Doppler Vibrometry system. (b) The frequency response test setup for the proposed 1D structure, suspend horizontally and excited with shaker. (c) Schematics of a 1D infinite periodic phononic structure, a primitive unit cell and the associated reduced Brillouin zone. (d-e) Band structure diagram of a 1D structure (left) and the frequency–dependent transmittance (right) obtained experimentally on a 4-unit cell sample of the structure with inactive and active magnetic elements. The colored insets show the exaggerated deformations of the unit cell and sample structure.

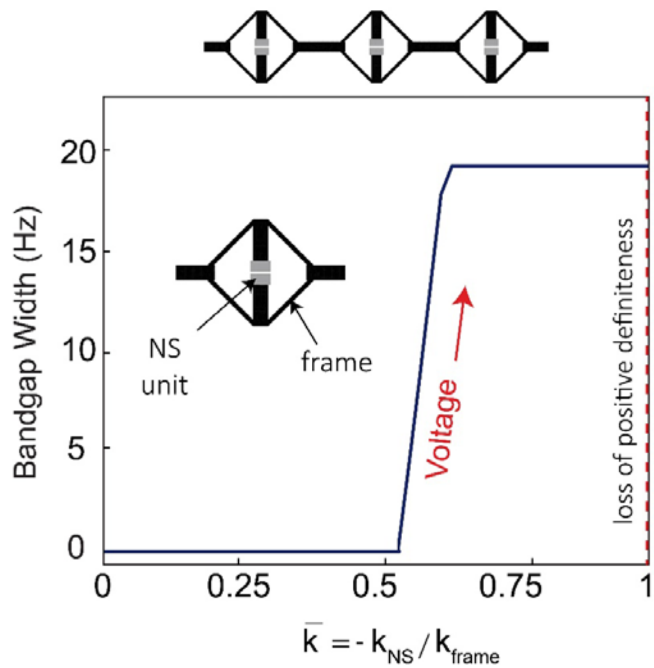

Figure 4: Evolution of phononic band gap width in the proposed 1-D tessellation as a function of the normalized value of negative stiffness between the electromagnets in the unit cell.

To corroborate the numerical results, a prototype of the 1D structure was manufactured (Figure 5) and its vibration transmittance was experimentally measured. Permanent magnets (N50 1/2"x1/4"x1/4" Neodymium Rare Earth Block Magnets, CMS Magnetics Company) were used in this study instead of the electromagnets for the sake of simplicity. The periodic 1D lattice, containing four unit cells, was fabricated through laser cutting of a 3/16" sheet of cast acrylic using a Trotec Speedy 360 laser cutter with laser wavelength of 630-680 nm and maximum laser beam power of 1mW. The dimensions of the structure were selected based on the attraction force of the magnets (depicted as red rectangles in Figure 5) and the stiffness of the acrylic base material. The experimental setup is shown in Figure 3b. The sample was suspended in air using thin, flexible strings and excited from one side using a LabWorks axial shaker and amplifier (Model ET-132 and PA-119) in the frequency range of 0 to 300 Hz. The frequency response of the proposed structure was measured using a 3D Laser Doppler Vibrometer (PSV 500) as shown in Figure 3a, in the X, Y, and Z directions. Several scanning points were used to accurately measure the full-field vibration in both the time and frequency domain. The frequency response of all the scan points were measured, and the average displacement of the scan points near the shaker (excited side) and the average displacement of the scan points on the opposite side of the structure (free side) were recorded. Transmittance was determined as the logarithm of the ratio of the vibration amplitude on the free side to that of the excided side. Negative transmittance with high decay corresponds to band gap. The performance of the structure was experimentally evaluated in two different scenarios: (i) with the magnets press-fitted inside the rectangular slots representing the 'Active' state; (ii) with non-magnetic steel parts with equal size and almost equal density as the magnets fitted in the slots to keep the overcall mass of the structure unchanged from case (i) ('Inactive' state).

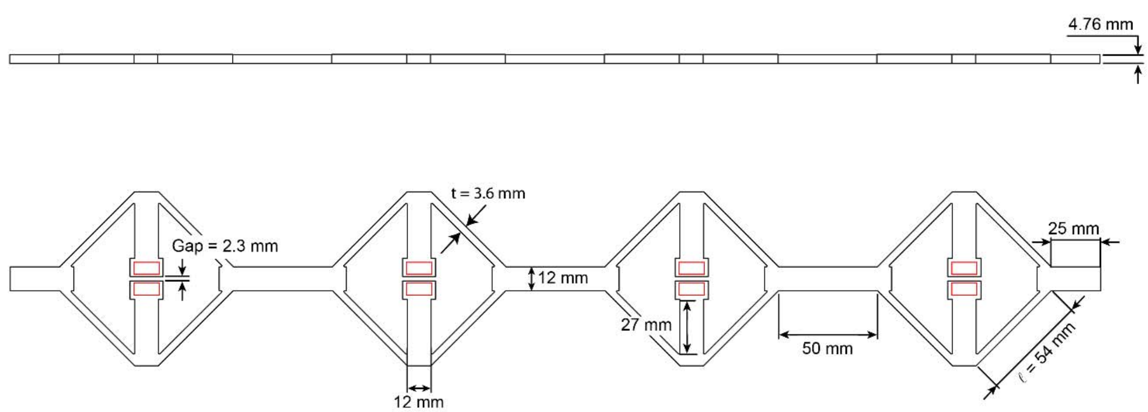

Figure 5. The dimensions of 1D structure fabricated by Laser cutting.

The results indicate a frequency range of strong attenuation around ~250 Hz in the structure without magnets, and one around ~150 Hz in the structure with magnets. The vibration isolation at ~250 Hz and ~150 Hz in the structures without and with magnets, respectively, can also be observed in the scaled-up deformation of the sample at each of these frequencies (Video 1-4). The slight discrepancies observed in the locations of the bandgaps captured from the FE models and the experiments are attributed to manufacturing imperfections (in particular variability in the wall thickness, which results in stiffness differences from cell to cell), and the low number of the unit cells used in the experiments (most studies of 1D phononic structures have been conducted on at least 5-6 unit cells [24, 25, 53]). Nonetheless, in spite of these slight discrepancies, these experiments clearly show that even a system with four unit cells allows us to strongly manipulate the band structure (and in particular the band gap location and width) by controling the negative stiffness elements within the material. In the presented color spectrum, the smallest and largest displacements are represented by red and blue colors, respectively. Note that here band gaps are created by changing the resonating frequency of the entire unit cell, rather than creation of the local resonance units (the observed band gap frequencies are an order of magnitude lower than the standalone local resonance of vertical bars around 800 Hz). It is also important to note that the low frequency bandgap shown in Figure 3e is obtained at a NS which is smaller than the overall stiffness of the polymeric structure. As discussed above, at a NS intensity of the electromagnets equal to only ~65% of the (positive) stiffness of the polymeric frame, the apexes of the dispersion curves for the quasi-longitudinal and quasi-transverse waves coincide. Further increase in NS intensities after this critical value does not lead to an increase in the width of the phononic band gap.

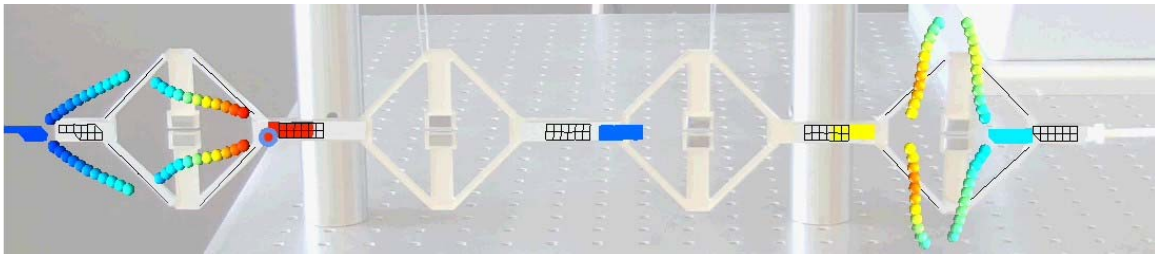

Video 1. Frequency response of the 1D structure without magnet at 143 Hz.

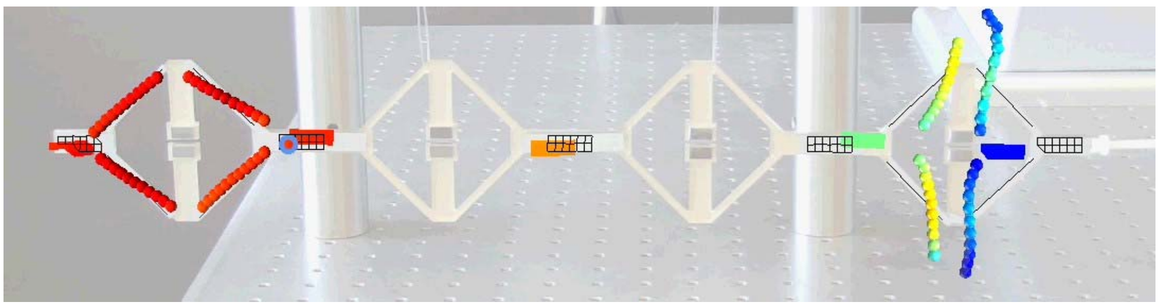

Video 2. Frequency response of the 1D structure without magnet at 255 Hz.

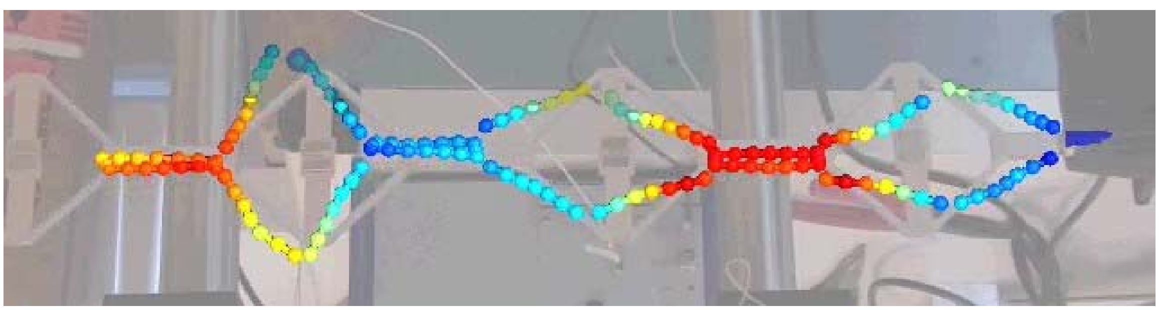

Video 3. Frequency response of the 1D structure without magnet at 143 Hz.

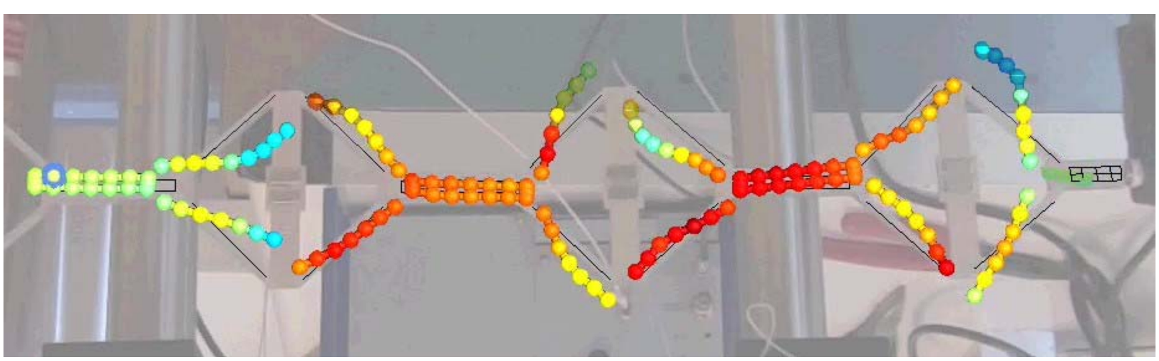

Video 4. Frequency response of the 1D structure without magnet at 255 Hz.

3.2 Two-dimensional tessellation

The 1D tessellation presented in Figure 3c encompasses NS inclusions that reduce the stiffness of the material in one direction (i.e. X). As a result, this architected material can only lead to modification of the dispersion curve for quasi-longitudinal low-frequency waves. A simultaneous lowering of the dispersion curves for both longitudinal- and transverse- dominated modes, however, could *potentially* lead to increased width of the introduced band gaps. As explained before, lowering all types of dispersion curves could also lead to a decrease in achievable band gap due to band degeneracies, making the determination of a proper strategy for creating phononic band gaps frequency- and structure-specific. A possible architecture to reduce material stiffness in multiple directions simultaneously, affecting propagating phononic waves of different polarizations, is the 2D triangular arrangement shown in Figure 6a. Here, we uniformly reduce the intensity of all electromagnets at various orientations, affecting the stiffness of material equally in all in-plane directions, while preserving linear elastic isotropy of the inactive material through geometrical symmetries[54]. Primitive cells of the structure and the associated Brillouin zone are shown in Figure 6a. The numerically obtained band diagrams of the lattices, for both the inactive and active states, are shown in Figure 6b. The frequencies are normalized by $\sqrt{k/m}$, where k is the stiffness of the frame and m is the mass of the electromagnets [29]. At the extreme NS intensity shown in Figure 6c, the dispersion curve corresponding to a quasi-transverse polarization becomes tangent to the horizontal axis, indicating that the material is at the onset of elastic instability (a band approaching $\omega = 0$ at a non-zero wave vector $\boldsymbol{k}$ is a common criterion used to detect the onset of buckling with wavelength given by $2\pi/k$ [55–57]). There are certain distinctions between the results presented in Figures 3 and 6. First, in the 2D lattice all polarizations of propagating waves, especially those in the low frequency range, are influenced by activation of NS elements (in other words, the Poisson's ratio is not near zero). Second, a gradual increase in NS intensity monotonically increases the band gap width until material instability is reached. The substantial band gap opening that results is due to the fact that the optical modes are largely unaffected by the stiffness change.

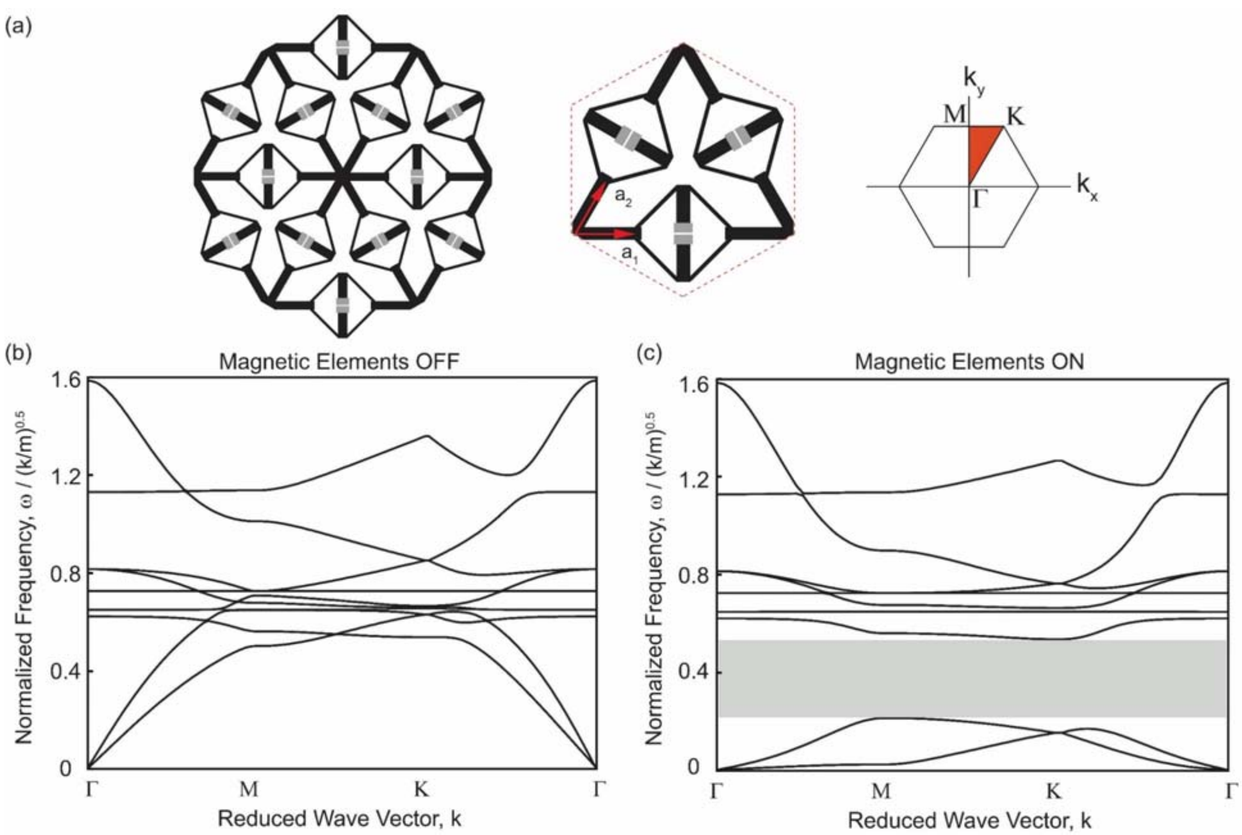

Figure 6. (a) Schematics of a 2D infinite periodic phononic structure (left), a primitive unit cell (middle), and the associated Brillouin zone (right). (b-c) Band structure diagram of the material obtained numerically for inactive and active states.

4. Conclusions

In summary, we proposed a novel pathway for convenient, real-time introduction and modification of extremely low frequency band gaps in phononic crystals. This was achieved by reducing the resonating frequencies of the unit cell of the phononic crystal, which will in turn lead to downshifting of the acoustic modes (<1000 Hz) without substantially affecting the optical modes. The evolution of band gaps can be explained through emergence of low-energy deformation modes due to introduction of NS inclusions. Specifically, the lowest dispersion branches of a material, corresponding to quasi-transverse and longitudinal waves, were modulated through reduction of material stiffness in specific directions. A 1D periodic structure was shown to allow suppression of longitudinal waves, and a 2D architecture was presented for suppression of both shear and longitudinal waves. We believe that the presented mechanistic model is able to correctly explain the following observed physical phenomena corresponding to the evolution of phononic band gaps in these phononic materials: i) selective suppression of quasi-longitudinal and transverse waves, shown in Figure 3, and ii) unaffected dispersion relations for high frequency waves in the proposed materials.

In closing, we note that in this manuscript we only investigated one-way tunability, whereby the voltage of the electromagnets (and hence the stiffness of the NS phase) is varied independently on environmental stimuli and a gap shift is detected (see Figure S2 in the supplementary information). In the experiments, permanent magnets are used in lieu of electromagnets in order to simplify the fabrication and experimental validation. Nonetheless, the ambitious, long-term vision for the proposed metamaterial concept is to ultimately enable real-time band gap manipulation by active control of the negative stiffness elements. Strategies for active control of band gap are currently under investigation.

Acknowledgments

This work was financially supported by Office of Naval Research (program Manager: D. Shifler, Contract # N00014-11-1-0884) and National Science Foundation (awards # 1401575 and 1401496). The Abaqus® Finite Element Analysis software is licensed from Dassault Systemes SIMULIA, as part of a Strategic Academic Customer Program between UC Irvine and SIMULIA. Ladan Salari-Sharif is grateful to Polytec Inc, specifically Kasra Kakavand, Mario Pineda, Jerome Eichenberger for providing us access to their PSV-500 system. We are also thankful to Prof. Stefano Gonella for insightful discussions.

References

[1] M. Maldovan and E. Thomas, *Periodic Materials and Interference Lithography for Photonics, Phononics and Mechanics*, (**2015**).

[2] F. Romeo and M. Ruzzene, Wave propagation in linear and nonlinear periodic media: analysis and applications, 326 (2013).

[3] P. A. Deymier, *Acoustic metamaterials and phononic crystals*, (**2013**).

[4] D. Caballero, J. Sánchez-Dehesa, C. Rubio, R. Mártinez-Sala, J. V. Sánchez-Pérez, F. Meseguer, and J. Llinares, Large two-dimensional sonic band gaps, Phys. Rev. E **60**, R6316 (1999).

[5] C. M. Anderson and K. P. Giapis, Larger Two-Dimensional Photonic Band Gaps, 2949 (1996).

[6] R. Martínez-Sala, J. Sancho, J. V. Sánchez, V. Gómez, J. Llinares, and F. Meseguer, Sound attenuation by sculpture, (1995).

[7] X. Zhang, Z.-Q. Zhang, L.-M. Li, C. Jin, D. Zhang, B. Man, and B. Cheng, Enlarging a photonic band gap by using insertion, Phys. Rev. B **61**, 1892 (2000).

[8] Z. Liu, X. Zhang, Y. Mao, Y. Y. Zhu, Z. Yang, C. T. Chan, and P. Sheng, Locally resonant sonic materials, Science **289**, 1734 (2000).

[9] G. Wang, X. Wen, J. Wen, L. Shao, and Y. Liu, Two-dimensional locally resonant phononic crystals with binary structures, Phys. Rev. Lett. **93**, 1 (2004).

[10] D. Cardella, P. Celli, and S. Gonella, Manipulating waves by distilling frequencies: A tunable shunt-enabled rainbow trap, Smart Mater. Struct. **25** (2016).

[11] P. Celli and S. Gonella, Manipulating waves with LEGO® bricks: A versatile experimental platform for metamaterial architectures, Appl. Phys. Lett. **107** (2015).

[12] A. Khelif and A. Adibi, Editors, *Phononic Crystals: Fundamentals and Applications*, Springer (**2015**).

[13] S. A. Cummer and D. Schurig, One path to acoustic cloaking, New J. Phys. **9** (2007).

[14] M. Kafesaki, M. M. Sigalas, and N. Garcia, Frequency modulation in the transmittivity of wave guides in elastic-wave band-gap materials, Phys. Rev. Lett. **85**, 4044 (2000).

[15] A. Khelif, A. Choujaa, S. Benchabane, B. Djafari-Rouhani, and V. Laude, Guiding and bending of acoustic waves in highly confined phononic crystal waveguides, Appl. Phys. Lett. **84**, 4400 (2004).

[16] T. Elnady, A. Elsabbagh, W. Akl, O. Mohamady, V. M. Garcia-Chocano, D. Torrent, F. Cervera, and J. Sánchez-Dehesa, Quenching of acoustic bandgaps by flow noise, Appl. Phys. Lett. **94**, 1 (2009).

[17] F. Casadei, L. Dozio, M. Ruzzene, and K. A. Cunefare, Periodic shunted arrays for the control of noise radiation in an enclosure, J. Sound Vib. **329**, 3632 (2010).

[18] D. Elser, U. L. Andersen, A. Korn, O. Glöckl, S. Lorenz, C. Marquardt, and G. Leuchs, Reduction of guided acoustic wave brillouin scattering in photonic crystal fibers, Phys. Rev. Lett. **97**, 1 (2006).

[19] L. Feng, X. P. Liu, M. H. Lu, Y. Bin Chen, Y. F. Chen, Y. W. Mao, J. Zi, Y. Y. Zhu, S. N. Zhu, and N. Ben Ming, Refraction control of acoustic waves in a square-rod-constructed tunable sonic crystal, Phys. Rev. B - Condens. Matter Mater. Phys. **73**, 2 (2006).

[20] C. Luo, S. G. Johnson, J. D. Joannopoulos, and J. B. Pendry, All-angle negative refraction without negative effective index, Phys. Rev. B **65**, 201104 (2002).

[21] M. Kafesaki, M. M. Sigalas, and E. N. Economou, Elastic wave band gaps in 3-D periodic

polymer matrix composites, Solid State Commun. **96**, 285 (1995).
[22] M. S. Kushwaha, P. Halevi, L. Dobrzynski, and B. Djafari-Rouhani, Acoustic band-structure of periodic elastic composites., Phys. Rev. Lett. **71**, 2022 (1993).
[23] C. Goffaux and J. Vigneron, Theoretical study of a tunable phononic band gap system, Phys. Rev. B **64**, 1 (2001).
[24] S. Babaee, N. Viard, P. Wang, N. X. Fang, and K. Bertoldi, Harnessing Deformation to Switch on and off the Propagation of Sound, Adv. Mater. **28**, 1631 (2016).
[25] P. Wang, F. Casadei, S. Shan, J. C. Weaver, and K. Bertoldi, Harnessing Buckling to Design Tunable Locally Resonant Acoustic Metamaterials, **014301**, 1 (2014).
[26] J. H. Jang, C. Y. Koh, K. Bertoldi, M. C. Boyce, and E. L. Thomas, Combining Pattern Instability and Shape-Memory Hysteresis for Phononic Switching, Nano Lett. **9**, 2113 (2009).
[27] S. Babaee, P. Wang, and K. Bertoldi, Three-dimensional adaptive soft phononic crystals, J. Appl. Phys. **117**, 244903 (2015).
[28] Y. Zárate, S. Babaee, S. H. Kang, D. N. Neshev, I. V Shadrivov, K. Bertoldi, and D. A. Powell, Elastic metamaterials for tuning circular polarization of electromagnetic waves, Sci. Rep. **6**, 28273 (2016).
[29] M. Schaeffer and M. Ruzzene, Wave propagation in reconfigurable magneto-elastic kagome lattice structures, J. Appl. Phys. **117** (2015).
[30] J. F. Robillard, O. B. Matar, J. O. Vasseur, P. A. Deymier, M. Stippinger, A. C. Hladky-Hennion, Y. Pennec, and B. Djafari-Rouhani, Tunable magnetoelastic phononic crystals, Appl. Phys. Lett. **95**, 2 (2009).
[31] O. Bou Matar, J. F. Robillard, J. O. Vasseur, A. C. Hladky-Hennion, P. A. Deymier, P. Pernod, and V. Preobrazhensky, Band gap tunability of magneto-elastic phononic crystal, J. Appl. Phys. **111** (2012).
[32] Y. Z. Wang, F. M. Li, W. H. Huang, X. Jiang, Y. S. Wang, and K. Kishimoto, Wave band gaps in two-dimensional piezoelectric/piezomagnetic phononic crystals, Int. J. Solids Struct. **45**, 4203 (2008).
[33] M. I. Hussein, M. J. Leamy, and M. Ruzzene, Dynamics of Phononic Materials and Structures: Historical Origins, Recent Progress, and Future Outlook, Appl. Mech. Rev. **66**, 040802 (2014).
[34] A. Sato, Y. Pennec, N. Shingne, T. Thurn-Albrecht, W. Knoll, M. Steinhart, B. Djafari-Rouhani, and G. Fytas, Tuning and switching the hypersonic phononic properties of elastic impedance contrast nanocomposites, ACS Nano **4**, 3471 (2010).
[35] K. L. Jim, C. W. Leung, S. T. Lau, S. H. Choy, and H. L. W. Chan, Thermal tuning of phononic bandstructure in ferroelectric ceramic/epoxy phononic crystal, Appl. Phys. Lett. **94**, 2007 (2009).
[36] L.-Y. Wu, W.-P. Yang, and L.-W. Chen, The thermal effects on the negative refraction of sonic crystals, Phys. Lett. A **372**, 2701 (2008).
[37] Zi-Gui Huang and Tsung-Tsong Wu, Temperature effect on the bandgaps of surface and bulk acoustic waves in two-dimensional phononic crystals, IEEE Trans. Ultrason. Ferroelectr. Freq. Control **52**, 365 (2005).
[38] E. R. G. Eckert and R. M. Drake, *Analysis of heat and mass transfer*, (**1987**).
[39] R. M. Bozorth, *Ferromagnetism*, Wiley-VCH (**1993**).
[40] P. L. Chu, P. Y. P. Chen, R. A. Sammut, and C. Science, Improving the linearity of piezoelectric ceramic actuators, Electron. Lett. **18**, 442 (1982).

[41] T. M. Proctor, An improved piezoelectric acoustic emission transducer Electrode element contac area surface, J. Acoust. Soc. Am. **1163** (1991).
[42] W. J. Drugan, Elastic composite materials having a negative stiffness phase can be stable, Phys. Rev. Lett. **98**, 1 (2007).
[43] D. M. Kochmann and W. J. Drugan, Analytical stability conditions for elastic composite materials with a non-positive-definite phase, Proc. R. Soc. A Math. Phys. Eng. Sci. **468**, 2230 (2012).
[44] R. S. Lakes and W. J. Drugan, Dramatically stiffer elastic composite materials due to a negative stiffness phase?, J. Mech. Phys. Solids **50**, 979 (2002).
[45] Z. Hashin, Analysis of properties of fiber composites with anisotropic constituents, J. Appl. Mech. **46**, 543 (1979).
[46] Z. Hashin and B. W. Rosen, The Elastic Moduli of Fiber-Reinforced Materials, J. Appl. Mech. 223 (1964).
[47] R. Hill, On uniqueness and stability in the theory of finite elastic strain, J. Mech. Phys. Solids **5**, 229 (1957).
[48] G. Geymonat, S. M??ller, and N. Triantafyllidis, Homogenization of nonlinearly elastic materials, microscopic bifurcation and macroscopic loss of rank-one convexity, Arch. Ration. Mech. Anal. **122**, 231 (1993).
[49] A. V. Pichugin and D. A. Prikazchikov, Remarks on explicit strong ellipticity conditions for anisotropic or pre-stressed incompressible solids: Table 1, Q. J. Mech. Appl. Math. **69**, 67 (2016).
[50] D. Han, H. H. Dai, and L. Qi, Conditions for strong ellipticity of anisotropic elastic materials, J. Elast. **97**, 1 (2009).
[51] J. L. Rose, *ultrasonic waves in solid media*, (**2000**).
[52] F. Bloch, ??ber die Quantenmechanik der Elektronen in Kristallgittern, Zeitschrift f??r Phys. **52**, 555 (1929).
[53] F. Javid, P. Wang, A. Shanian, and K. Bertoldi, Architected Materials with Ultra-Low Porosity for Vibration Control, Adv. Mater. 5943 (2016).doi:10.1002/adma.201600052
[54] A. E. H. Love, *A treatise on the mathematical theory of elasticity*, (**2013**).
[55] K. Bertoldi, M. C. Boyce, S. Deschanel, S. M. Prange, and T. Mullin, Mechanics of deformation-triggered pattern transformations and superelastic behavior in periodic elastomeric structures, J. Mech. Phys. Solids **56**, 2642 (2008).
[56] K. Bertoldi and M. C. Boyce, Wave propagation and instabilities in monolithic and periodically structured elastomeric materials undergoing large deformations, Phys. Rev. B 1 (2008).doi:10.1103/PhysRevB.78.184107
[57] X. Ning and S. Pellegrino, Bloch wave buckling analysis of axially loaded periodic cylindrical shells ψ Axis, Comput. Struct. **177**, 114 (2016).
[58] P. Wang, J. Shim, and K. Bertoldi, Effects of geometric and material nonlinearities on tunable band gaps and low-frequency directionality of phononic crystals, **014304** (2013).
[59] S. Shan, S. H. Kang, P. Wang, C. Qu, S. Shian, E. R. Chen, and K. Bertoldi, Harnessing multiple folding mechanisms in soft periodic structures for tunable control of elastic waves, Adv. Funct. Mater. **24**, 4935 (2014).
[60] M. S. Kushwaha, P. Halevi, L. Dobrzynski, and B. Djafari-Rouhani, Acoustic band structure of periodic elastic composites, **71**, 2022 (1993).
[61] Y. Tanaka and S. Tamura, Surface acoustic waves in two-dimensional periodic elastic structures, Phys. Rev. B **58**, 7958 (1998).

[62] X. Wang, X. Zhang, Q. Yu, and B. Harmon, Multiple-scattering theory for electromagnetic waves, Phys. Rev. B **47**, 4161 (1993).
[63] H. Y. D. Yang, Finite difference analysis of 2-D photonic crystals, Microw. Theory Tech. IEEE Trans. **44**, 2688 (1996).
[64] L. Brillouin, *Wave Propagation in Periodic Structures*, Dover, New York (**1953**).

Appendix 1 – Analytical model for magneto-elastic metamaterial design

In this section, simple analytical formulas are presented to express the overall stiffness of the tunable phononic lattices proposed in section 2 in terms of the geometric, elastic and electromagnetic properties. A unit cell of the structure is shown in Figure 2a. The unit cell embeds a pair of attracting electromagnets, which effectively functions as a mechanical spring with a negative spring coefficient between the two electromagnets. The overall stiffness of the deformed unit cell is determined by two components: (i) the stored elastic strain energy in the frame and (ii) the change in the magnetic potential energy between the two electromagnets. Linearizing the contributions of the elastic and magnetic components, the overall stiffness of the unit cell can be expressed in terms of the elastic stiffness of the frame and the tangential negative stiffness of the pair of electromagnets at the center of the unit cell.

The distance between the electromagnets in the frame in the inactive state is denoted by χ_0. When the electromagnets are activated, this distance is reduced to χ_f, where the magnetic attraction and the elastic force exerted by the frame to the electromagnets are in equilibrium. Around this equilibrium state, the derivative of the electromagnetic force with respect to distance is denoted by k^*, which represents the (negative) stiffness created by the pair of electromagnets. Also, around this equilibrium state, the values of elastic stiffness of the frame in x and y are denoted by K_x and K_y, which can be expressed in terms of geometrical parameters of the frame as follows:

$$\begin{aligned} K_y &= \frac{12EI}{\ell^3 \cos^2 \theta} \\ K_x &= \frac{12EI}{\ell^3 \sin^2 \theta} \end{aligned} \tag{3}$$

In obtaining these values, Euler–Bernoulli beam assumption is adopted, and furthermore the effect of the initial deformation of the frame due to electromagnetic forces is neglected. Using Castigliano's theorem, the overall stiffness of the unit cell is obtained as:

$$K_x^{eq}(V) = K_x\left(1 - \frac{k^*}{K_y}\right) \tag{4}$$

where I, ℓ are the second moment of area and the length of the bars constituting the frame, respectively, E is the stiffness of the constituent material, and θ is the angle of the bars with respect to the horizontal line. Note that for $\theta = 45^o$, K_x is equal to K_y. From Eq. (4), one can see that if $k^* = K_x$ the overall stiffness of the structure, K_{eq}, is zero.

Even though in Eq. (4) the force-displacement profiles of both magnetic and elastic components are assumed linear, the magnetic force-displacement response between two attracting electromagnets has a highly nonlinear nature ($\frac{dF}{dx} \sim x^{-3}$), especially at close distances between the two electromagnets (i.e. $x \to 0$). Therefore, it is imperative to consider an entire range of nonlinear magnetic force-displacement response in order to find the equilibrium state between the elastic and magnetic components, or inversely, to find the initial state of the unit cell such that a near-zero stiffness for the structural unit cell is achieved by activation of the electromagnets. For a given geometry, a near-zero stiffness is obtained if the initial distance between the magnets χ_0 is such that (i) the magnetic and elastic forces between the pair of electromagnets after activation are equal, and (ii) the derivative of the magnetic force, $\frac{\partial F}{\partial x}$, at the equilibrium distance χ_f is equal to K_x (or $k^* = K_x$). These conditions can be mathematically expressed as:

$$\begin{aligned} F(\chi_f) &= K_x(\chi_o - \chi_f) \\ \left.\frac{\partial F}{\partial x}\right|_{x=\chi_f} &= K_x \end{aligned} \tag{5}$$

where $F(\chi)$ represents the nonlinear magnetic force between the two electromagnets as a function of their distance. The set of Eq. (2) can be also presented geometrically, as shown in Figure A1. Here, the green line represents the purely-elastic (i.e. electromagnets inactive) load-displacement response of the unit cell measured between the locations of the electromagnets. The magnetic force-distance response of the electromagnets for a given applied voltage is shown by the black curve. Zero-stiffness, albeit unstable, equilibrium is achieved in the unit cell through activation of the electromagnets, only if the initial gap between the two electromagnets χ_0 is designed to be equal to the x-intercept of a line of slope $-K_x$ tangent to the magnetic force – distance curve, as shown in this figure. This unstable equilibrium state is marked by an asterisk in this figure.

We experimentally measured the magnetic force-distance profile of the electromagnets used in this study. The pairs of electromagnets with an overall size of 34 mm x 18 mm (diameter x height) and weight of 90 gr, rated for 12V DC, purchased from Uxcell. To measure the force-displacement response, the electromagnets were screwed into two steel rods, which were in turn clamped to the tensile grips of a universal testing machine, Instron 8862 frame. During the test, the electromagnets were first snapped together, with the voltage turned on, and the electromagnets were quasi-statically separated while the force displacement data was recorded. This procedure was repeated for different applied voltages, from 4V to 12V with an increment of 2V. Figure 2b shows the attraction force between two electromagnets as a function of their distance for different applied voltages. By increasing the voltage, the force displacement response shifts to the upper right corner of the graph, resulting in higher attraction load for a given distance. The relation between the magnetic force, distance and voltage of the electromagnets can be approximated by:

$$F = \frac{cV^2}{(\mathrm{x}+\mathrm{a})^2} \tag{6}$$

Equation (3) was curve-fitted into the experimental data to determine constant *c* and *a*. The slope of a line tangent to the force displacement curve is calculated by differentiation of Eq. (4):

$$\partial F / \partial X = \frac{-2cV^2}{(\mathrm{x}+\mathrm{a})^3} \tag{7}$$

Using Eq. (1,2 and 4), the geometry of the frame including the initial gap χ_0, the frame wall thickness t, length, ℓ, angle θ, and out of plane thickness for a required overall material stiffness can be estimated from the values of applied voltage, unit cell dimensions, and constituent materials properties.

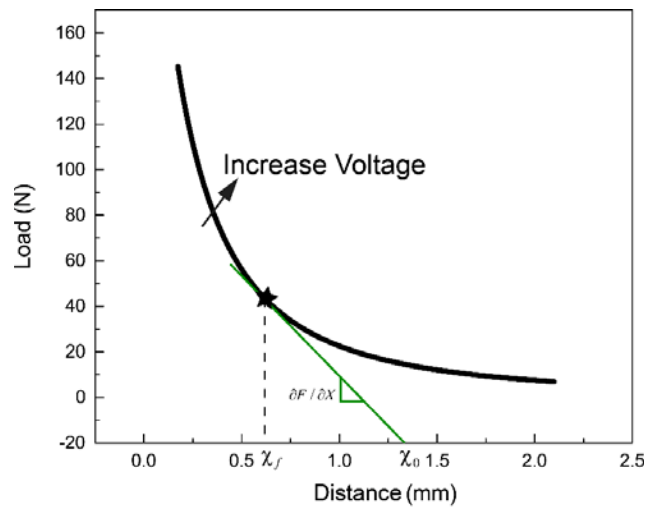

Figure A1. The magnetic force – distance curve (black) between the pair of electromagnets for an applied voltage of 12 V, and the tangent to this curve (green) used to obtain the final frame configuration (asterisk).

For fabrication of the unit cell shown in Figure 2a, a frame with dimensions $\ell = 50$ mm, $t = 3.7$ mm, $\theta = 45^\circ$, and depth of $w = 15$ mm was manufactured using FDM 3D printing. The base material was PLA, that has a Young's Modulus of $E = 1.9$ GPa. For the described unit cell, a near-zero stiffness is resulted for the values of applied voltage and electromagnets initial distance of 6V and $\chi_0 = 1.2$ mm, respectively.

Appendix 2 – Wave Propagation in Infinite Periodic Structures

In this appendix, an implementation of the Bloch-wave theorem[52] for obtaining the band structure of a phononic crystal through finite elements method is explained. This approach has been previously used by a number of researchers to predict the wave propagation response [22, 58] and instability [55, 59] in periodic structures. Here, we summarize this method for completeness. Besides the current implementation, other commonly used approaches for calculation of band structure in phononic and photonic crystals include the plane-wave expansion

(PWE) [60, 61], the multiple-scattering theory (MST) [61, 62], and the finite-difference (FD) [63] methods.

In infinite phononic crystals (including, 1D, 2D and 3D periodic structures), elastic waves do not propagate as plane waves, but they propagate as Bloch waves [52]. A Bloch wave can be described by the expression:

$$\boldsymbol{u}(\boldsymbol{x}, t) = \tilde{\boldsymbol{u}}(\boldsymbol{x}) e^{i(\boldsymbol{k}\cdot\boldsymbol{x} - \omega t)} \tag{8}$$

where $\boldsymbol{k}$ is the wave vector, inversely proportional in magnitude to the wavelength λ ($k = 2\pi/\lambda$), ω is the angular frequency, and $\tilde{\boldsymbol{u}}(\boldsymbol{x})$ is a periodic complex vector function with the same spatial periodicity as the phononic crystal. Therefore, for any pair of periodically located lattice points at a distance $\boldsymbol{R}$, we have:

$$\tilde{\boldsymbol{u}}(\boldsymbol{x} + \boldsymbol{R}) = \tilde{\boldsymbol{u}}(\boldsymbol{x}) \tag{9}$$

As $\boldsymbol{x}$ and $\boldsymbol{x}$+$\boldsymbol{R}$ are periodically located, for a 2D lattice we can express $\boldsymbol{R} = n_1\boldsymbol{a_1} + n_2\boldsymbol{a_2}$, with n_1 and n_2 arbitrary integers, and $\boldsymbol{a_1}$and $\boldsymbol{a_2}$ the primitive vectors of the lattice. In 2D, the *reciprocal* lattice primitive vectors are related to the lattice primitive vectors through the following relationships [1]:

$$\begin{aligned} \boldsymbol{b}_1 &= 2\pi \frac{\boldsymbol{a}_2 \times \hat{\boldsymbol{e}}_3}{\|\boldsymbol{a}_1 \times \boldsymbol{a}_2\|} \\ \boldsymbol{b}_2 &= 2\pi \frac{\hat{\boldsymbol{e}}_3 \times \boldsymbol{a}_1}{\|\boldsymbol{a}_1 \times \boldsymbol{a}_2\|} \end{aligned} \tag{10}$$

where $\hat{\boldsymbol{e}}_3 = \frac{\boldsymbol{a}_1 \times \boldsymbol{a}_2}{\|\boldsymbol{a}_1 \times \boldsymbol{a}_2\|}$. The set of all reciprocal lattice vectors (i.e., the set of vectors $\boldsymbol{G} = m_1\boldsymbol{b}_1 + m_2\boldsymbol{b}_2$, where m_1 and m_2 are any integers) denotes the entire set of wave vectors that can satisfy the periodicity of the lattice. The set of wave vectors, $\boldsymbol{k}$, required to completely describe the propagation of electromagnetic waves in two-dimensional photonic crystals is referred to as the Brillouin zone [1, 64]. The Brillouin zone for a 2D structure with cubic symmetry is shown in Figure 1a in the main manuscript.

Bloch waves propagating through a periodic isotropic elastic medium must satisfy the Navier's equation, namely:

$$\rho\ddot{\boldsymbol{u}} = (\lambda + \mu)\boldsymbol{\nabla}(\boldsymbol{\nabla} \cdot \boldsymbol{u}) + \mu\nabla^2\boldsymbol{u} \tag{11}$$

where λ and μ are the Lame's elastic constants of the material. Inserting the Bloch solution (Eq. (6) in the Navier's equation results in an eigenvalue problem that has non-trivial solutions only if the frequency ω and the wave vector $\boldsymbol{k}$ are in a particular relation, $\omega = \omega(\boldsymbol{k})$, called the *dispersion relation*. In an infinite lattice, the dispersion relation has infinitely many branches, called *modes* (corresponding to the eigenvalues of the problem). The set of frequency modes plotted along key directions in the Brillouin zone is called the *band diagram*. For a square 2D lattice (depicted in Figure 1) with cubic symmetry, the tip of the wave vectors $\boldsymbol{k}$ should follow the ΓXMΓ path, representing the outlines of the irreducible Brillouin zone. For triangular lattice with the six folds symmetry, the Brillouin zone is hexagonal shaped (Figure 4) and the wave vector, $\boldsymbol{k}$, follows the ΓKMΓ path.

This eigenvalue problem can be discretized and solved with the Finite Element method on a primitive cell. In the commercial FE software ABAQUS, this can be done using the Eigenfrequency solver. To implement the complex-valued Bloch boundary conditions (Eq. 6), two identical numerical parts with the same geometry and mesh were constructed, one representing the real part and the other the imaginary part of the solution. The equations for the

Bloch-periodic displacement boundary conditions can be also divided into two sets of uncoupled equations for the real and imaginary parts:

$$\begin{aligned}\mathrm{Re}(\boldsymbol{u}^{B_i}) &= \mathrm{Re}(\boldsymbol{u}^{A_i})\cos[\boldsymbol{k}\cdot\boldsymbol{r}_{A_iB_i}] - \mathrm{Im}(\boldsymbol{u}^{B_i})\sin[\boldsymbol{k}\cdot\boldsymbol{r}_{A_iB_i}]\\ \mathrm{Im}(\boldsymbol{u}^{B_i}) &= \mathrm{Re}(\boldsymbol{u}^{A_i})\sin[\boldsymbol{k}\cdot\boldsymbol{r}_{A_iB_i}] + \mathrm{Im}(\boldsymbol{u}^{B_i})\cos[\boldsymbol{k}\cdot\boldsymbol{r}_{A_iB_i}]\end{aligned} \tag{12}$$

where $\boldsymbol{r}_{A_iB_i} = \boldsymbol{x}^{B_i} - \boldsymbol{x}^{A_i}$ denotes the distance in the current/deformed configuration between the two nodes A_i and B_i periodically located on the boundaries of the unit cell. These boundary conditions can be easily assigned through the "Equation" subroutine in ABAQUS/Standard.

For FE discretization of the phononic response, numerical models of the 2D crystals were meshed using 4 node bilinear plane stress quadrilateral elements with reduced integration and hourglass control (CPS3). To verify the experimental results, the base material of the frame was modeled as a linear elastic isotropic material with $\rho = 1180\ \mathrm{kg/m^3}$ and $E = 3.2\ \mathrm{GPa}$, corresponding to cast Acrylic base material. The electromagnetic interactions between the pair of electromagnets within the unit cell were modeled through elastic axial connectors with negative stiffness which are extended between the parallel inside surfaces of the two attracting electromagnets. The negative stiffness connector is swept incrementally from $-K_x$ to zero with increments of $K_x/50$, where K_x is the (positive) stiffness of the frame measured between the connector ends. A negative stiffness connector with zero stiffness, represents a pair of "inactive" or non-interacting electromagnets, and a negative stiffness connector with stiffness $-K_x$ corresponds to a zero net stiffness albeit mechanically unstable frame.